Spatiotemporal Modeling of the Wind Field over an Urban Lake Subject to Wind Sheltering

MOHAMMAD ASHRAFI,[a] LLOYD H. C. CHUA,[b] K. N. IRVINE,[a] AND PEIPEI YANG[c]

[a] *National Institute of Education, Nanyang Technological University, Singapore*
[b] *School of Engineering, Faculty of Science, Engineering and Built Environment, Deakin University, Waurn Ponds, Victoria, Australia*
[c] *Nanyang Environment and Water Research Institute, Nanyang Technological University, Singapore*

(Manuscript received 18 February 2021, in final form 20 November 2021)

ABSTRACT: The wind field over an urban lake may exhibit considerable variability resulting from wind-shielding effects from surrounding structures. Field measurements at an urban reservoir in Singapore were augmented by computational fluid dynamics (CFD) model results to develop a wind model over the reservoir surface via a data assimilation approach. The field measurements identified, depending on structure alignment with the prevailing wind direction, wind shielding that impacted wind direction and velocity over the reservoir surface. The wind model integrated the temporal response of the measurements and spatial distribution produced by the CFD modeling. The wind model was used to predict the spatiotemporal pattern of the wind field over the reservoir surface for a full year. The modeling results showed good agreement with measured wind data at three measurement locations on the reservoir surface. The wind model has been incorporated with a hydrodynamics and water quality model to provide the spatiotemporal wind forcing over the reservoir surface.

KEYWORDS: Monsoons; Wind; In situ atmospheric observations; Instrumentation/sensors; Surface observations; Statistical techniques; Time series; Data assimilation; Urban meteorology

1. Introduction

Lakes are often at risk from natural and anthropogenic stresses that can lead to toxic algal bloom and fish kills (Irvine et al. 2003; Kangur et al. 2016, 2013; Moss et al. 2011; Murphy et al. 2003; Randall and Tsui 2002; Zhu et al. 2008). This risk can be greater for urban lakes, which tend to be smaller and shallower, with a high degree of exposure to anthropogenic activities (Schueler and Simpson 2001). Urban lakes are also susceptible to wind-sheltering effects from surrounding structures, which can lead to decreased wind stress acting on the lake surface, thereby reducing mixing energy, increasing stability, and creating potential for water quality degradation. In cities where such lakes are sited in commercial or residential areas and are designed as water features, there are also economic and social considerations for proper water management. The combined impacts of high exposure and reduced mixing would imply that, in the modeling of urban lakes, it is important to represent the wind field acting on the lake surface in a more realistic manner.

The wind field is required as a surface boundary condition for modeling, and shielding effects need to be considered when prescribing the wind stress acting on the water surface. The direction and velocity of wind over a lake surface are governed by surrounding elements such as vegetation canopy, topography, and buildings. Studies of waterbodies have shown that consideration of variable wind conditions produced by coastal forests and steep slopes can improve modeling of lake circulation patterns (Podsetchine and Schernewski 1999; Rubbert and Köngeter 2005). Hipsey et al. (2004) revealed that downwind velocity deficits of small, wind-sheltered waterbodies in Western Australia could eventually lead to a 20%–30% reduction in evaporation. As seen in Rueda et al. (2005), considerable variability in the wind field over Clear Lake, California, occurred as a result of the local topography. In another study, Markfort et al. (2010) used a wind tunnel to examine bluff/vegetation canopy effects in a lake and validated their results against field measurements. Both laboratory and field investigations suggested reduction of shear stress over a longitudinal distance of 40–60 times the canopy height. The study also showed substantial wind sheltering occurred in lakes smaller than 1 km^2 in size that are surrounded by bluffs or tree canopies taller than 10 m.

In modeling lake hydrodynamics, the wind field can be treated in a variety of ways. The simplest method is to define a uniform wind field such as investigations for Lake Ypacarai, Paraguay (Alexander and Imberger 2009; Imberger et al. 2017); Lake Okeechobee, Florida (Jin and Ji 2004); and Lake Tianyinhu, Nanjing, China (Gong et al. 2016). Some studies (Hodges et al. 2000; Laval et al. 2003; Marti and Imberger 2008; Marti et al. 2016; Valerio et al. 2012) have employed a simple linear interpolation method to capture the wind field variability. Laval et al. (2003) indicated that although a uniform wind field applied in a lake model simulated the internal wave motions well, the simulated seiche amplitudes were too large. However, prescription of a variable wind field improved the wave amplitude prediction and reduced the phase (timing) error significantly. Valerio et al. (2012) concluded that "internal wave modes are excited whenever the spatial and temporal structure of a wind field over a lake matches the surface velocity field of a

Irvine's current affiliation: Faculty of Architecture and Planning, Thammasat University, Khlong Luang, Pathum Thani, Thailand.

Corresponding author: Mohammad Ashrafi, mashrafi.eng@gmail.com

DOI: 10.1175/JAMC-D-21-0027.1

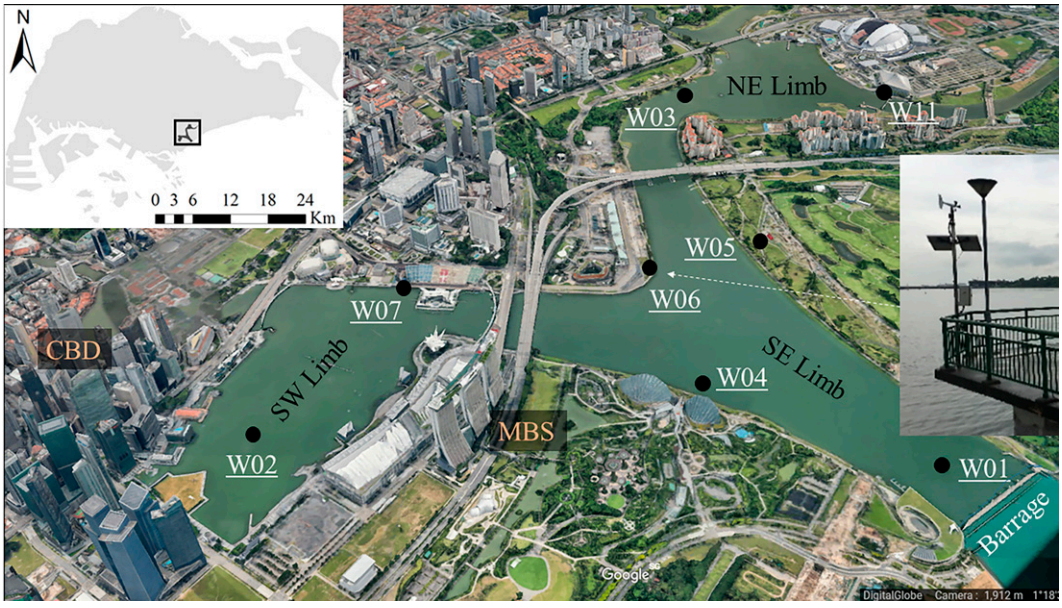

FIG. 1. A 3D image of the study site (Google Earth 2017) showing the reservoir in downtown Singapore, flanked by tall structures.

particular internal mode." Gong et al. (2016) used the 3D Environmental Fluid Dynamics Code to study an urban lake, Lake Tianyinhu, in the southeast of Nanjing, China. Dissolved oxygen, chlorophyll a, total phosphorus, total nitrogen, and ammonia nitrogen (NH_4) were modeled with uniform wind applied at the lake surface. Xing et al. (2018) applied the Estuary Lake and Coastal Ocean Model (ELCOM) coupled with the Computational Aquatic Ecosystem Dynamics Model (CAEDYM) for a tropical reservoir in Singapore. The effects of variable versus uniform wind field on water quality were investigated, and it was found that application of a variable wind field provided more accurate modeling results, particularly for the areas of the reservoir affected by wind shielding from the surrounding buildings.

The above review highlights the importance of accurately representing the spatial characteristics of a wind field on hydrodynamic and water quality model results. In addition, for real-time management, the temporal dimension needs to be considered. We applied field measured wind data and adapted results from a computational fluid dynamics (CFD) model for an urban lake to develop a model to predict the spatiotemporal wind field. Although it might be possible to run the CFD model directly to predict the wind field, this option is infeasible due to the run time and computation requirements (Hendricks et al. 2007), since a secondary goal of the model is that it should be suitable for real-time implementation, which requires model run time to be within reasonable limits. Therefore, the objectives of this study were to (i) analyze field measured wind data for temporal behavior at several locations around a highly urbanized reservoir, (ii) assimilate CFD model results for the steady wind field over the lake, and (iii) develop an algorithm to couple the field measured temporal data with steady-state CFD model results to predict spatiotemporal wind patterns.

2. Method

A data assimilation technique that incorporates field measured wind data and CFD modeled data is proposed in this study. First, the wind data measured at the reference station (located at the reservoir surface, free from obstructions) was analyzed for the average wind speed for 10 dominant wind directions. Second, a CFD model was run for each of the average wind speeds at these 10 wind directions to generate maps of the spatially varying wind field over the entire reservoir surface. The CFD model was run for steady conditions. Third, additional maps of the wind field corresponding to other wind velocities were generated. Using the 10 CFD wind fields from the previous step, a database of 30 maps per wind direction corresponding to other wind velocities, or a total of 300 maps were created via a scaling procedure. Last, a data assimilation procedure was applied incorporating the temporal wind data measured at the wind stations and the CFD wind field database in developing the spatiotemporal wind model. The accuracy of the spatiotemporal wind model was validated by comparing the model results with field data.

a. Study area and field data

The study site is a tropical reservoir in Singapore (Fig. 1). The reservoir is divided into three limbs, namely, the southwest (SW), northeast (NE), and southeast (SE) limbs. The SW limb of the reservoir is mostly flanked by tall buildings, with the central business district (CBD) area to the west that hosts some of the tallest buildings in Singapore, with the tallest buildings averaging 230 m in height and in excess of 60 stories. Likewise, the NE limb is flanked by tall residential apartments to the south. The SE limb is the most open and less impacted by structures.

Singapore has a tropical climate characterized by warm temperatures, high humidity, and abundant rainfall throughout

the year. Average temperatures range from 24° to 32°C during the night and day, respectively. Relative humidity ranges from 90% in the early morning to 60% in the midafternoon. Rain is recorded on an average of 167 days per year with a long-term mean annual rainfall of 2166 mm. The climate in Singapore can be characterized by two monsoon seasons. The northeast monsoon (NEM) season occurs from December to early March with prevailing northerly to northeasterly winds. Although rainfall occurs throughout the year, December and January are typically the wettest months. The southwest monsoon (SWM) season lasts from June to September with prevailing southeasterly to southerly winds. During this season, thunderstorms originating from Sumatra or the Straits of Malacca may cause occasional wind gusts from predawn to midday. The periods between the two dominant monsoon seasons are referred to as the intermonsoon (IM) periods (from late March to May and again in October and November), and these two intermonsoons generally have less-distinctive wind patterns (Meteorological Service Singapore 2018).

Two-dimensional (2D) wind sensors (R. M. Young 2020) were installed to collect wind data at a total of eight locations (W01–W07 and W11 in Fig. 1) in the vicinity of the reservoir. Wind sensors W01, W02, W03, and W04 were deployed on platforms floating on the reservoir surface, with W03 and W04 closer to shore and W01 and W02 farther out in open water. W05, W06, W07, and W11 were located onshore, close to the edge of the reservoir and sited close to large buildings so as to understand the impact to the wind field from these structures. The shore-based wind sensors were installed at a height of approximately 2 m above ground. Each sensor recorded wind direction and velocity at 1-min intervals. The floating sensors also incorporated compass readings to correct for sensor motion. W01 was adopted as the reference station since it is located on the water surface and is relatively unaffected by obstructions while measurements by the other wind sensors were expected to be influenced by adjacent structures. Wind data over a full year, from 0000 LT 16 January 2014 to 2359 LT 15 January 2015, were analyzed in this study. In addition, wind data were also available for 2007 at W01. This additional set of wind data was analyzed (see wind model and analysis of wind data; section 2c and 3a, respectively) to provide the boundary condition for the CFD model. All the wind data were first cleaned by removing duplicate values and outliers and filling missing data. A number of methods have been identified to infill missing time series data in the literature, including regression, inverse distance weighting, nonparametric stochastic direct sampling, neural network, and other artificial intelligence approaches (Coulibaly and Evora 2007; Dembélé et al. 2019; Nourani et al. 2016; Shabalala et al. 2019; Tardivo and Berti 2012). However, because the data quality was reasonably good (only 8% were found to be erroneous, and most were single values) and because of the fine temporal resolution of the data, we took a simpler approach whereby single missing values were calculated using the average of the previous and next records. In cases for which there were missing consecutive values, we applied the value recorded exactly one cycle (i.e., 1 day or 1440 min) before. Furthermore, the data were also smoothed to remove noise, using the Savitzky–Golay filtering method (Orfanidis 1996), which adopts a best-estimate window size for noise cancellation. Other details of the wind data collection and analysis can be found in Du et al. (2014).

b. CFD model

Diagnosis of the wind field for steady conditions over the reservoir surface was conducted using a CFD model following the approach (Wang et al. 2017, 2020) of a previous study by Du et al. (2014). The CFD model used was Fluent (ANSYS 2019), which solves the incompressible continuity and momentum equations for turbulent flow. The k–ε model was adopted for turbulence closure because of its high computational efficiency (Anderson 1995). Standard and second-order discretization schemes were adapted for pressure interpolation. The boundary conditions used were (i) inlet condition, where the velocity and direction were determined from the analysis of the wind data measured at the reference station (see wind model section, section 2c); (ii) outlet boundary condition, where atmospheric pressure was specified; (iii) nonslip (wall boundary) condition adjacent to solid boundaries; and (iv) free-slip condition elsewhere. The area that was modeled included the reservoir and large buildings and structures extending approximately 3 blocks inland and measured 3.5 km × 2.5 km × 0.8 km high. The size of each computation cell is 20 m × 20 m, with a total of 40 million cells used for the entire modeled domain. Model runs were conducted on a 12-core, 32-GByte memory workstation with eight parallel Fluent licenses; each simulation took about 2 days to reach convergence to a steady state (ANSYS 2019; Du et al. 2014). The computed wind speeds and directions were extracted for development of the wind field database, as explained further in the description of the wind model (section 2c).

c. Wind model

The framework for a real-time high-resolution wind model for the reservoir was initially proposed in Du et al. (2014) and tested for a limited time period. Further developments of the initial model are reported in this paper, including development of the model for long-term simulation of the spatiotemporal variability of the wind field suitable for real-time application. The wind model integrates the temporal wind variations continuously measured at a given number of locations with the spatial wind variations over the entire reservoir surface, obtained from the CFD model. The wind model thus evaluates the wind velocity and direction at any location of the reservoir surface, taking as inputs, data measured at chosen sensor locations. This optimal interpolation (Daley 1991) is similar to common spatial modeling approaches (Krause et al. 2006; Wu et al. 2012), where the target variable can be simulated at unobserved locations provided variables of interest are measured at sensors placed at selected locations.

A flowchart explaining the wind model workflow is provided in Fig. 2. The wind model is composed of three major parts, detailed in six steps. The first two parts, the reference station data analysis and generation of wind maps, focus on spatial modeling, while the third or model operation part focuses on spatial–temporal integration. In reference station data analysis,

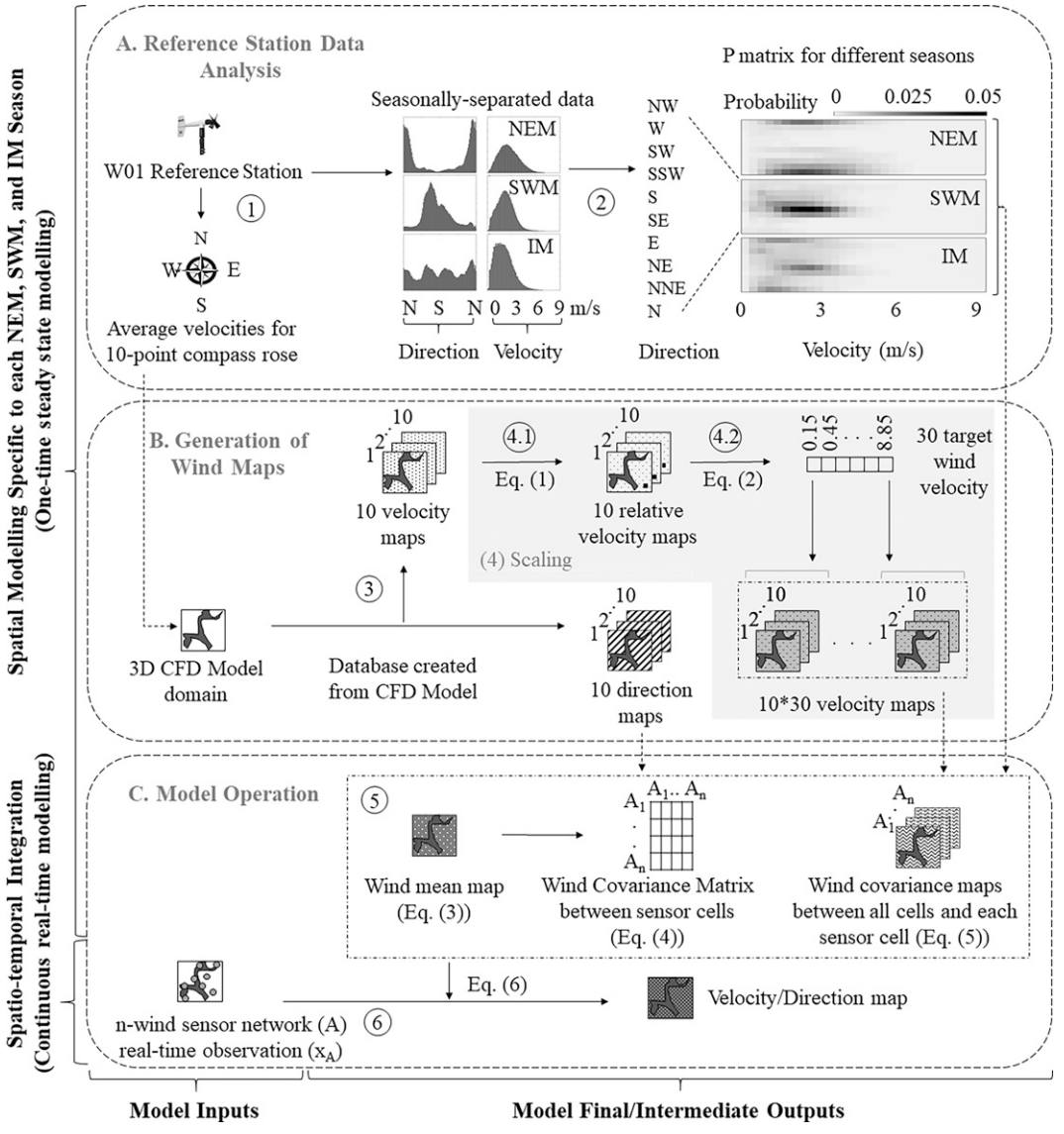

FIG. 2. Schematic of the wind model workflow for NEM, SWM, and two IM seasons. The individual model steps are denoted by numbers within open circles.

wind data measured at the reference station W01 were analyzed to provide the reference wind speeds and directions and their probability of occurrence for the NEM, SWM, and the two IM seasons. In generation of wind maps, CFD model results were analyzed to provide the spatial distribution of wind over the water surface. Finally, model operation integrates the real-time wind data recorded at selected locations with the spatial model for the NEM, SWM and the two IM seasons. Following this general description, details of each of the steps are as follows:

In step 1 (reference station data analysis), the wind data for 2007 at W01 were binned according to an 8-point compass rose. Two more directions, north-northeast (NNE) and south-southwest (SSW), were included in the analysis, yielding a 10-point compass rose in total.

In step 2 (probability of occurrence), the data at W01 were also analyzed to provide a probability of occurrence (**P**) matrix. The reference station wind speed can reach a maximum of 9 m s^{-1}. For each of the compass rose directions, therefore, the wind speed was divided into 30 segments in bins of 0.3 m s^{-1}, with midpoints equal to $V_R' = 0.15, 0.45, 0.75, \ldots, 8.85$ m s^{-1}. This results in a 10×30 matrix, with each cell containing a distribution of wind speeds over a specified direction range. The probability of occurrence was derived by counting the number of instances in each cell of the matrix divided by the total number of instances.

In step 3 (CFD model simulations), the average wind speed V_R from the reference station (W01) was derived for each of the 10-point compass directions (step 1) and applied

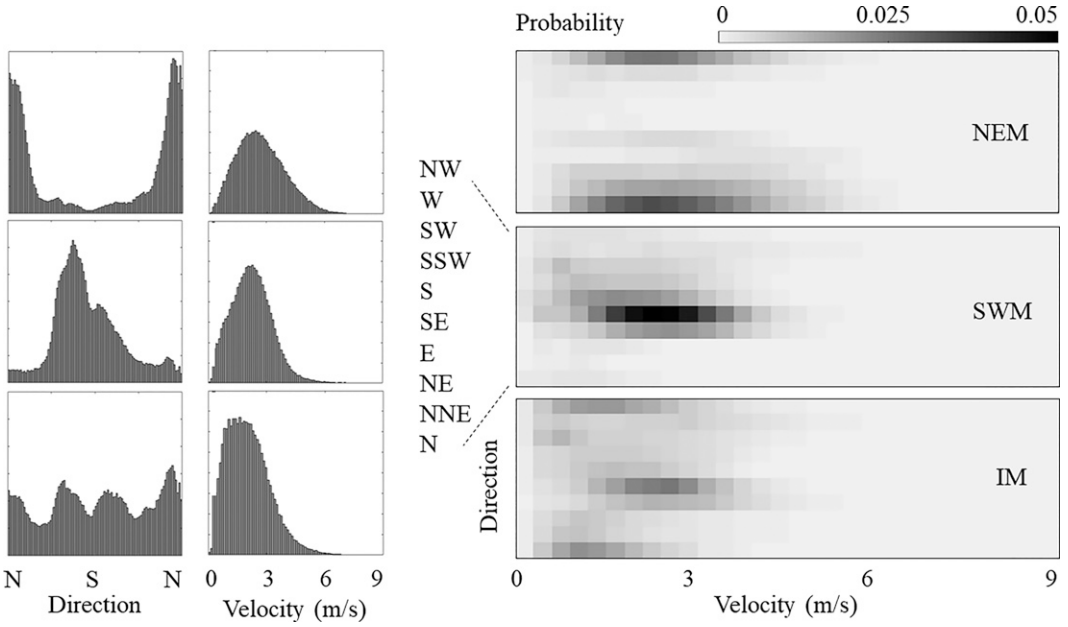

FIG. 3. Wind data for 2007 at W01.

to the CFD model as the inlet boundary condition. Because of the high computational cost of running CFD models (Hendricks et al. 2007), the model was run to steady state for only the average wind condition. The CFD model runs resulted in 10 velocity maps, corresponding to the 10 compass directions.

In step 4 (scaling), the velocity maps created in step 3 are gridded cells that cover the reservoir, with each cell containing wind speed and direction. These velocity maps, however, are applicable to only the average wind speed at the reference station $\overline{V}_R$ for each compass rose direction. This is obviously insufficient, since in practice, the wind speed will vary over a range of values. As it was computationally prohibitive to run the CFD model for all reference station wind speeds, a linear scaling approach was used to approximate the velocity distributions over the entire reservoir surface at other reference station wind speeds. Considering all the cells covering the reservoir ϑ, the computations were done for each individual cell υ. First, a relative velocity at each cell V'_υ was created (see step 4.1 in Fig. 2) by normalizing the CFD model result for each cell V_υ with the CFD model result at the reference station $\overline{V}_R$:

$$V'_\upsilon = V_\upsilon / \overline{V}_R. \tag{1}$$

Then, the velocity map for other values of V'_R at the reference station were obtained by scaling:

$$V_{\upsilon R} = V'_\upsilon V'_R, \tag{2}$$

resulting in 30 velocity maps for each compass point direction (see step 4.2 in Fig. 2). This process was repeated for the 10-point compass rose directions, resulting in 300 velocity maps.

In step 5 (mean and covariance computations), the average wind velocity at each cell μ_υ can be computed as

$$\mu_\upsilon = \sum_{k=1}^{300} x_{\upsilon k} P_k, \tag{3}$$

where $x_{\upsilon k}$ is the wind velocity at cell υ captured from wind velocity map k (k = 1, 300) and P_k is the corresponding probability of occurrence. In Eq. (3), the velocity was first converted from a polar coordinate system to a Cartesian one (Stull 2017), such that μ_υ represents either the eastward (U) or northward (V) velocity components. If $\mathbf{A} \subset \vartheta$ is a vector containing n wind station cells, the covariance of wind velocity between wind station cells $\mathbf{\Sigma_{AA}}$ can be computed as

$$\mathbf{\Sigma_{AA}} = \begin{bmatrix} \Sigma_{1,1} & \cdots & \Sigma_{1,n} \\ \vdots & \ddots & \vdots \\ \Sigma_{n,1} & \cdots & \Sigma_{n,n} \end{bmatrix}, \tag{4}$$

where $\Sigma_{i,j} = \mathrm{cov}(x_i, x_j) = \sum_{k=1}^{300} P_k \left(x_{ik} - \mu_i\right)\left(x_{jk} - \mu_j\right)$; x_{ik} and x_{jk} are velocities at wind stations i and j, respectively, captured from velocity map k; and μ_i and μ_j are mean velocities at a wind stations i and j. The covariance of wind velocity between each cell υ and the wind station cells $\mathbf{\Sigma_{\upsilon A}}$ can be computed as

$$\mathbf{\Sigma_{\upsilon A}} = \begin{bmatrix} \Sigma_{\upsilon,1} & \cdots & \Sigma_{\upsilon,n} \end{bmatrix}, \text{ and}$$

$$\Sigma_{\upsilon j} = \mathrm{cov}(\upsilon, j) = \sum_{k=1}^{300} P_k \left(x_{\upsilon k} - \mu_\upsilon\right)\left(x_{jk} - \mu_j\right), \tag{5}$$

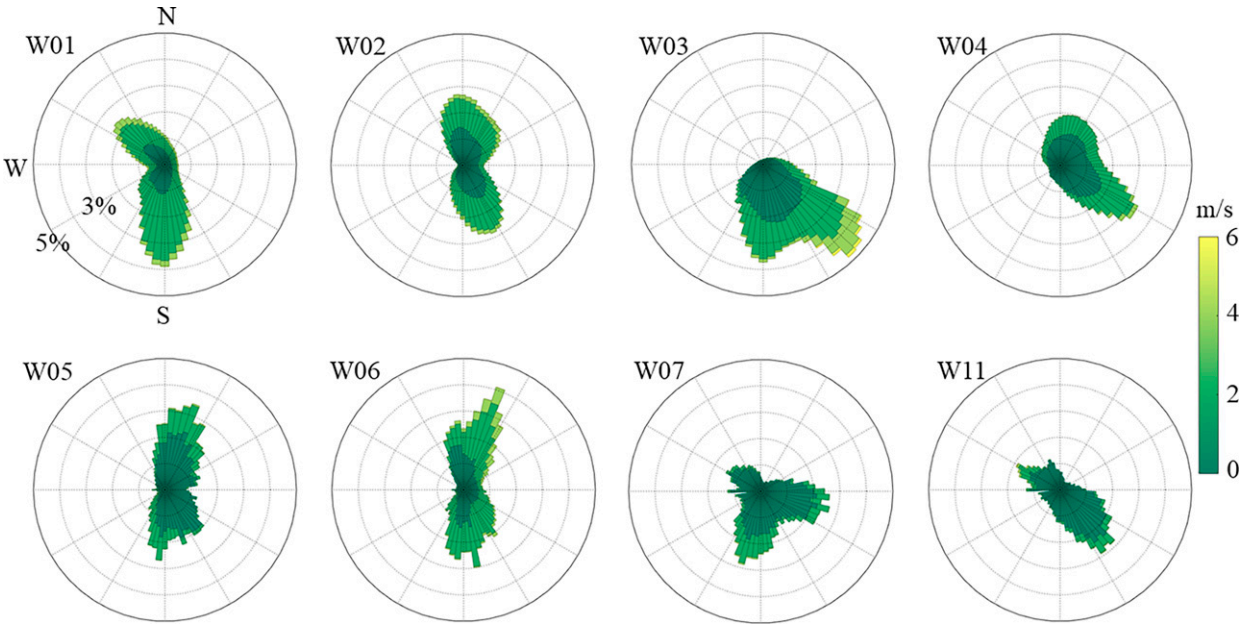

FIG. 4. Wind roses for all stations, 2014–15.

where x_{vk} is the wind velocity at cell v. For each velocity and direction, Eq. (4) results in an n by n matrix, where n is wind station cells, and Eq. (5) results in n covariance maps, with each map showing the covariance of all cells with a specific wind station cell.

In step 6 (modeling of spatiotemporal patterns), the spatiotemporal pattern of the wind over the reservoir surface is determined from an integration of the real-time measured data with the mean μ_v maps, covariance maps $\mathbf{\Sigma}_{v\mathbf{A}}$, and covariance matrix $\mathbf{\Sigma}_{\mathbf{AA}}$:

$$\mu_{(v|\mathbf{A})} = \mu_v + \mathbf{\Sigma}_{v\mathbf{A}}\mathbf{\Sigma}_{\mathbf{AA}}^{-1}(\mathbf{x}_\mathbf{A} - \mu_\mathbf{A})^{\mathrm{T}}, \tag{6}$$

where $\mu_{(v|\mathbf{A})}$ is the modeled wind at cell v and $\mathbf{x}_\mathbf{A}$ is the vector of real-time wind sensor readings.

3. Results and discussion

a. Analysis of wind data

The probability density function of the 2007 wind data for the reference station W01 is shown in Fig. 3. The recorded data show that the wind direction tracks in general northerly and southerly directions during the NEM and SWM seasons, respectively, and is more variable during the two IM seasons. Karthikeya et al. (2016) indicated that the measured wind direction can deviate significantly from the prevailing wind directions even when measurements were made on rooftops of the tallest buildings in the study area. The average wind speed recorded at W01 for 2007 was used for the CFD model (step 1 wind model section; section 2c) and computation of the probability matrix (step 2 wind model section; section 2c). The probability of occurrence for 10 different wind directions partitioned into 30 bins with 0.3 m s^{-1} intervals is also shown. The probability distributions indicate higher probabilities in N and SE directions for NEM and SWM seasons, respectively, and that higher magnitude winds occur mainly in the NEM season.

The wind data recorded at per minute intervals for 2014–15 at all the wind stations (a total of 525 600 data points per station) are shown in Fig. 4 and indicate seasonal variations in wind direction and velocity for the NEM, SWM, and IM seasons. Similar to the 2007 data, the wind recorded at W01, is mainly in the north (N) and south (S) directions. There is a significant degree of spatial heterogeneity in both the wind speed and direction caused by obstructions around the reservoir. The W02, W05, and W06 sites generally exhibit northerly and southerly directions for the NEM and SWM seasons, respectively. Site W03 shows significant alteration to the wind characteristics during the NEM season, and this can be attributed to obstructions close to W03, which resulted in the wind direction being deflected in a southeasterly direction during NEM season. The data measured at site W07 are affected during both the NEM and SWM seasons by tall buildings located north and south of W07, respectively (Fig. 1). Likewise, the wind velocity recorded at W11, which is flanked by a sports stadium to the north and high-rise apartment buildings to the south, is markedly low.

The hourly variation for the 2014–15 data is plotted as 24-h ensembles for different seasons in Fig. 5. Irrespective of the season, it is observed that wind velocities are generally weaker in the morning and peak around midafternoon. There is better agreement between the measured wind direction and the expected wind direction for the NEM than the SWM seasons, since winds from the south approach the reservoir relatively unhindered. The wind direction recorded at W01

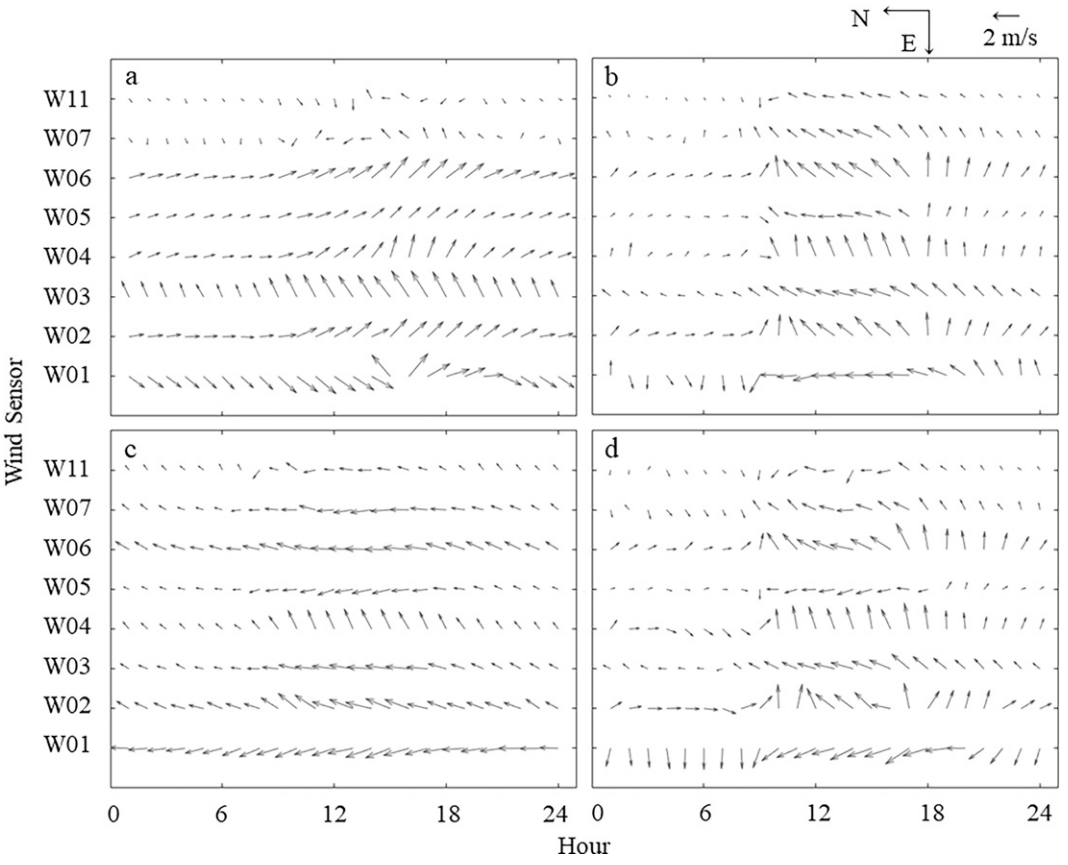

FIG. 5. Diurnal variation of wind direction and velocity for different seasons: (a) NEM, (b) IM 1, (c) SWM, and (d) IM 2. Note that wind vectors are plotted with 0° (N) pointing toward the left (←), proceeding in counterclockwise direction, with 90° (E) pointing downward (↓), etc.

exhibits mainly northerly and southerly directions consistent with the NEM and SWM seasons, respectively, with greater variability during the IM seasons. Wind velocities recorded at W07 and W11 are noticeably lower than at other locations due to shielding by surrounding structures. Alterations to the wind direction measured at W03, particularly during the NEM season as a result of the elevated highway north of W03, are also apparent.

b. CFD model results

Figure 6 shows the wind velocities obtained from the 10 CFD model runs with wind originating from the 10 compass points, or N, NNE, NE, E, SE, S, SSW, SW, W, and NW directions, with average speeds of 2.0, 2.1, 1.7, 2.5, 2.3, 1.6, 1.5, 1.0, 1.9, and 1.8 m s^{-1}, respectively. These speeds were obtained from the analysis of the 2007 wind data at W01, shown in Fig. 3. In general, the results show that wind speeds decrease significantly in the wake region of large structures, accompanied by significant alteration in direction. For winds from the south, it is observed that the SW limb wind velocity falls close to 0 in the wake region, extending over the entire region to the north, due primarily to tall buildings south of the SW limb. The wind is also channeled between the buildings, reaching velocities of up to 1.7 m s^{-1} and giving rise to a high velocity gradient over the surface. Similar sheltering effects can be observed over parts of the NE limb due to high-rise apartments to the south. Last, little impact, if any, can be observed to the wind field over the SE limb (Fig. 1) as it is relatively free from structures. Similar observations are made for winds from the north (0°).

Results from the CFD model were analyzed corresponding to a further nine directions as mentioned in the wind model section (section 2c), with the severity of impact varying with wind direction and relative orientation to tall buildings. Figure 7 shows CFD model direction/velocity mean maps for different seasons (generated as detailed in step 5, wind model section, section 2c) The CFD model output shows that alteration of the wind condition over the reservoir surface varies between the different seasons, especially in the SW limb. The SW limb is fronted by tall buildings to the north and south. The locations of these buildings coincide with the dominant wind directions during the main monsoon seasons, inducing a wake zone over the water surface of the SW limb through the year. On the other hand, the wind field in the NE limb is relatively unaffected during the NEM season but altered during the SWM season.

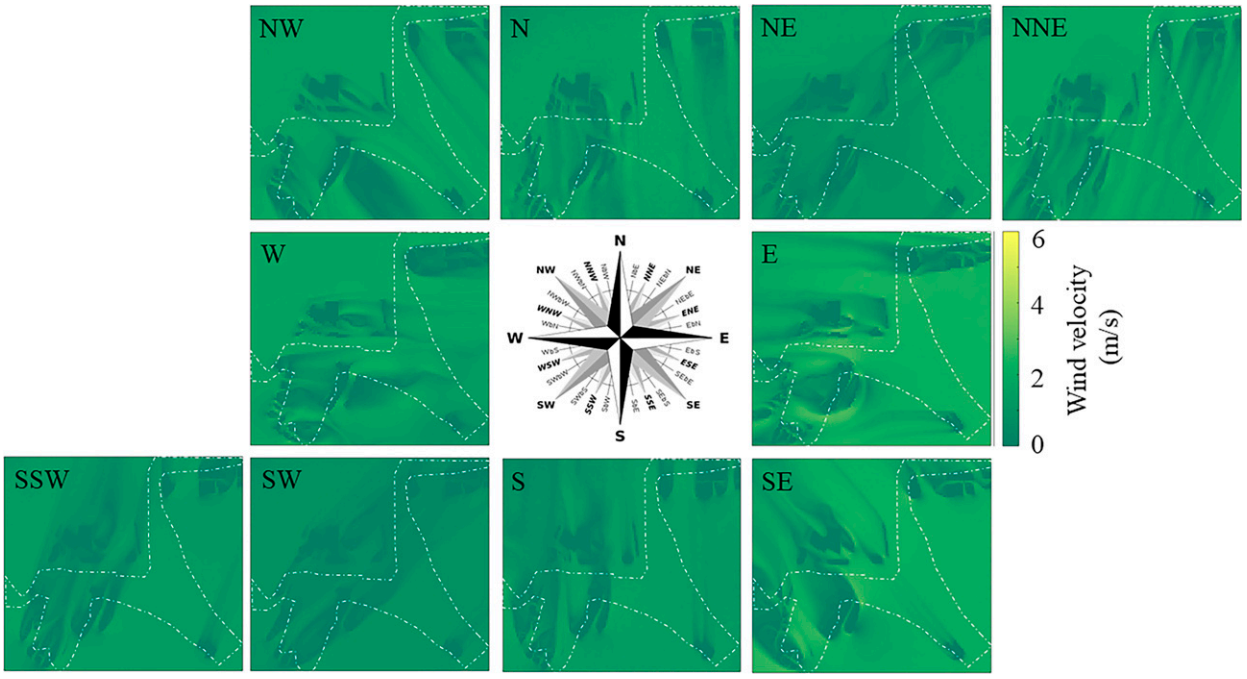

FIG. 6. CFD model results for 10 dominant wind directions (the reservoir is enclosed by the white dashed line).

Figure 8 illustrates the covariance matrix of the sensor network for each season. The figure shows that the covariance between each pair of sensors is positive, indicating the tendency of a linear relationship between sensors. Lower covariance (e.g., for sensor W02 or sensor W07 with other sensors) specifically in NEM season, may relate to the fact that W02 and W07 are in the reservoir SW limb, which is most impacted by the presence of tall buildings and therefore experiences the greatest degree of alteration to its wind field.

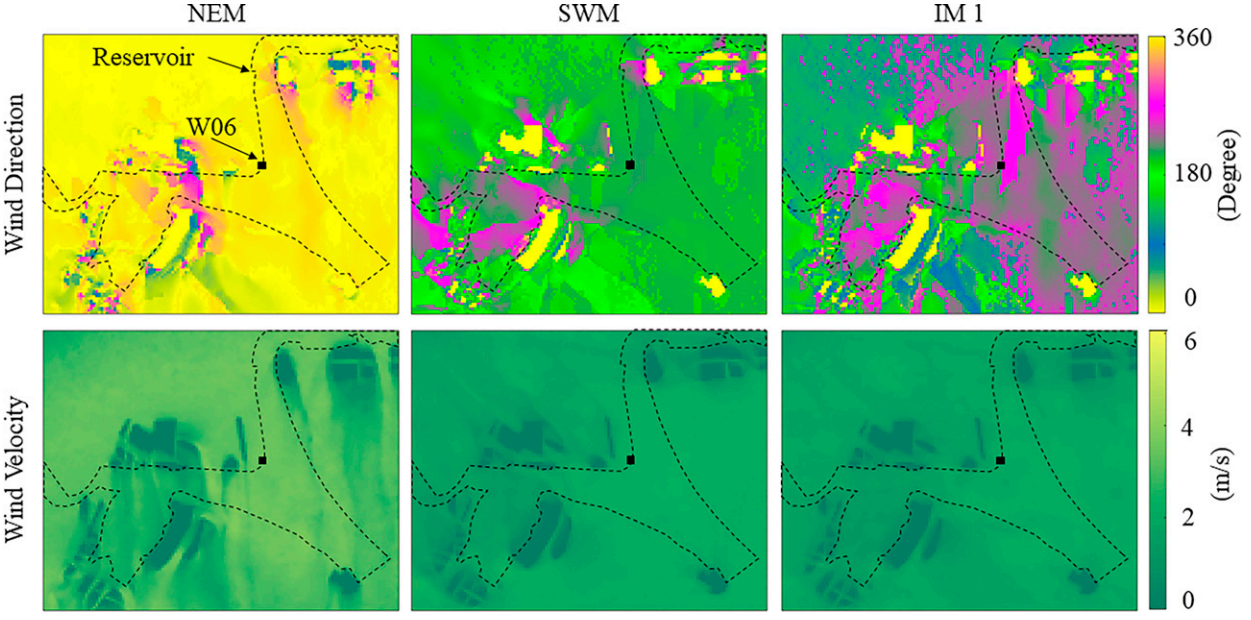

FIG. 7. CFD model direction/velocity mean maps for different seasons (the reservoir is enclosed by the black dashed line).

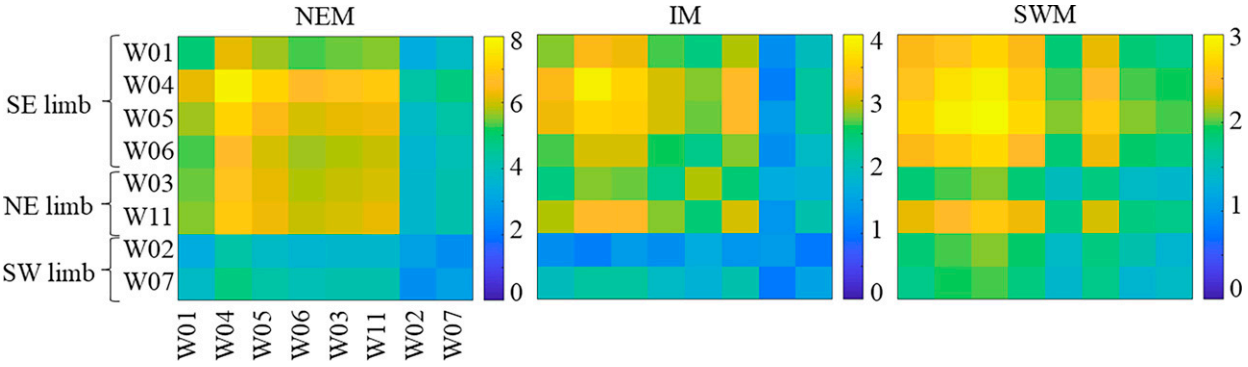

FIG. 8. Covariance matrix of wind sensor network for different seasons.

c. Spatiotemporal wind model

1) MODEL VALIDATION AND CHOICE OF SENSORS

In the development of the spatiotemporal wind model [Eq. (6)], field measured wind data is required. Our inspection of the wind sensor data shows that most of the land-based sensors (W05, W07, and W11) are locally impacted by structures close by; data from these sensors hence have a higher variability relative to the reservoir-based sensors. It is uncertain if the inclusion of the data from the onshore sensors will be detrimental in real-time predictions, due to the high degree of variability in the data. A sensitivity study therefore was carried out to determine the location and number of wind sensors ($\mathbf{x_A}$) to be included in the wind model. Another reason for selecting candidate wind sensors is eventually the selected sensors will be included in the real-time system, and this investigation was needed to identify the most appropriate combination of sensors to be used. Two scenarios were thus evaluated: scenario 1, applying all land- and reservoir-based sensors, except W06; scenario 2, applying only the reservoir-based sensors W01, W02, W03, and W04. The two scenarios were validated by comparing the results with wind measured at W06, which was averaged over 10 min from 0000 LT 16 January 2014 to 2359 LT 15 January 2015. The scenario that provides the better validation of the spatiotemporal model would then be selected for the real-time system.

Comparisons of the wind model results with measured data at W06 are shown in Fig. 9. An observation of the results indicates that scenario 2 provides a better agreement between the measured and predicted results. In general, the R^2 for wind speed prediction is much higher for scenario 2 than for scenario 1; R^2 is 0.4 versus 0.28 for NEM, 0.5 versus 0.22 for SWM, and 0.65 versus 0.29 for IM. These results indicate that the wind sensors placed on the water surface are better for real-time predictions. It is apparent that the shore-based wind sensors, such as W05, W07, and W11 located close to structures are sensitive to local fluctuations, whereas the reservoir-based sensors provide an integrative effect combining perturbations to the wind field exerted by buildings close to the shore. Including shore-based sensors presents an over refinement of the wind inputs required by the model, leading to a deterioration in model results.

2) LONG-TERM MODEL EVALUATION

The CFD database and the probability matrix (steps 1–4, wind model section; section 2c) were used to provide the mean maps, covariance matrix between sensor cells, and covariance maps between each cell and the sensor network for modeling the spatiotemporal wind variations (step 5 of wind model section; section 2c), suitable for real-time application. Figure 10 illustrates a snapshot, at noon, of results from the real-time wind model for a given day of each season. The wind model results for the NEM season (Fig. 10b) show a general direction of NNE mainly over the SE limb. However, there is some alteration to the prevailing wind direction in the SW and NE limbs due to the tall buildings around the reservoir. The wind velocity is generally higher in the SE limb, reaching up to 5.4 m s^{-1}, and generally there are higher velocities at the southeast half of the SE limb. The SW limb is in a sheltered area with reduced velocities except at the eastern and western edges of the Marina Bay Sands (MBS), where velocity can increase to 5 m s^{-1} because of winds passing the outermost edges of high-rise buildings in the CBD area, accompanied by change in wind direction (Fig. 10a). In the NE limb, the wind velocity is likewise relatively smaller than that for the SE limb.

The wind model results for the SWM season are shown in Figs. 10e and 10f (15 August 2014). Wind directions are generally from 180° with the exception of areas adjacent to the tall buildings south of the SW limb (Fig. 1), where wind direction is dramatically altered, winds in excess of 5 m s^{-1} are observed around the buildings, and velocities are substantially reduced in the wake region. Although a large variation is observed in the SW limb, the wind velocity is almost uniform in the SE limb (Fig. 10e). For the NE limb, velocities are lower, generally, as compared with the SE limb because of the wind-sheltering effect of the apartments south of the NE limb. The wind model results for IM seasons (30 April and 15 October 2014) are generally less distinct (Figs. 10c,d,g,h, respectively). Velocity during the IM season in the SE limb is slightly lower than during the monsoon seasons. For the NE limb the wind is also uniform and has a lower velocity relative to the SWM season.

A full year variation of the wind at the water surface at three selected locations in the reservoir (SE limb, SW limb,

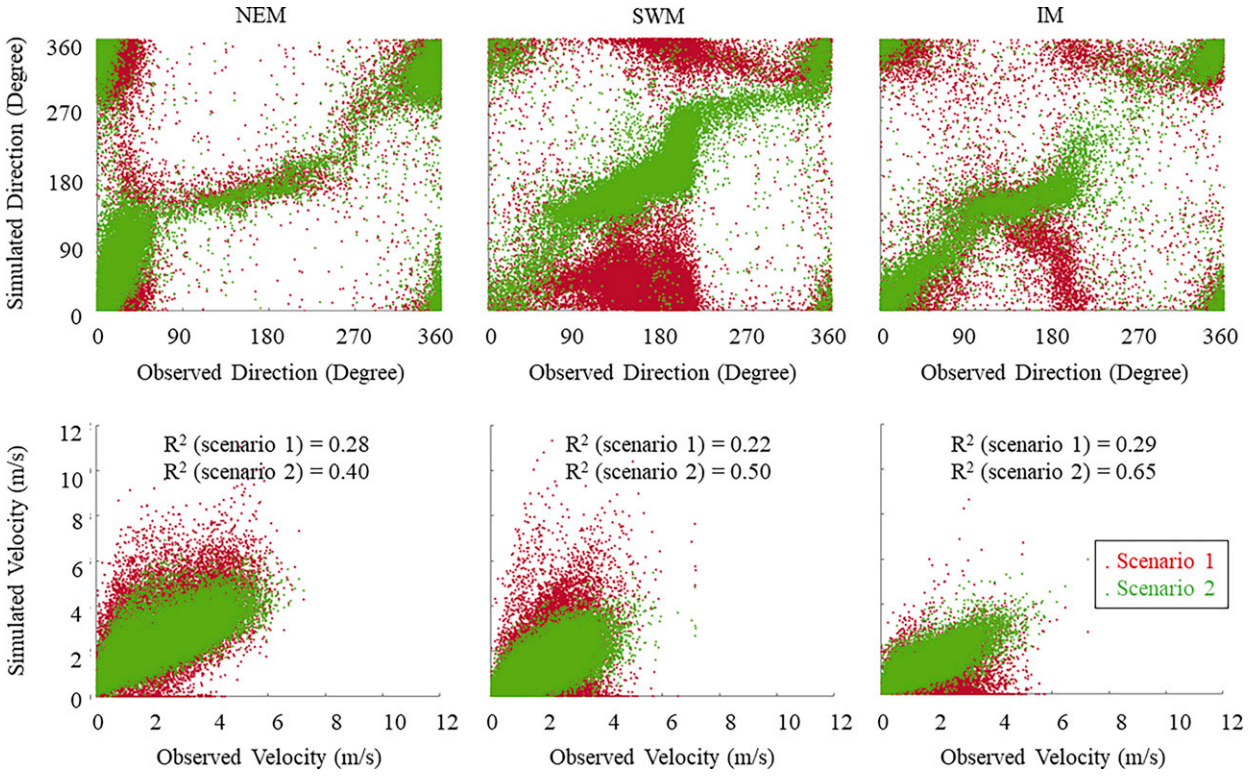

FIG. 9. Model results for the two scenarios.

and NE limb, as indicated in Fig. 10a) is shown in Fig. 11 for the period from 0000 LT 16 January 2014 to 2359 LT 15 January 2015. Results for the other 4150 locations on the reservoir surface can similarly be plotted. In deriving these plots, the wind model takes as input the wind data measured incrementally at the sensors, to generate the spatiotemporal distribution of the wind field over the water surface. Wind velocities in the SE and NE limbs (Figs. 11a,b) generally are higher

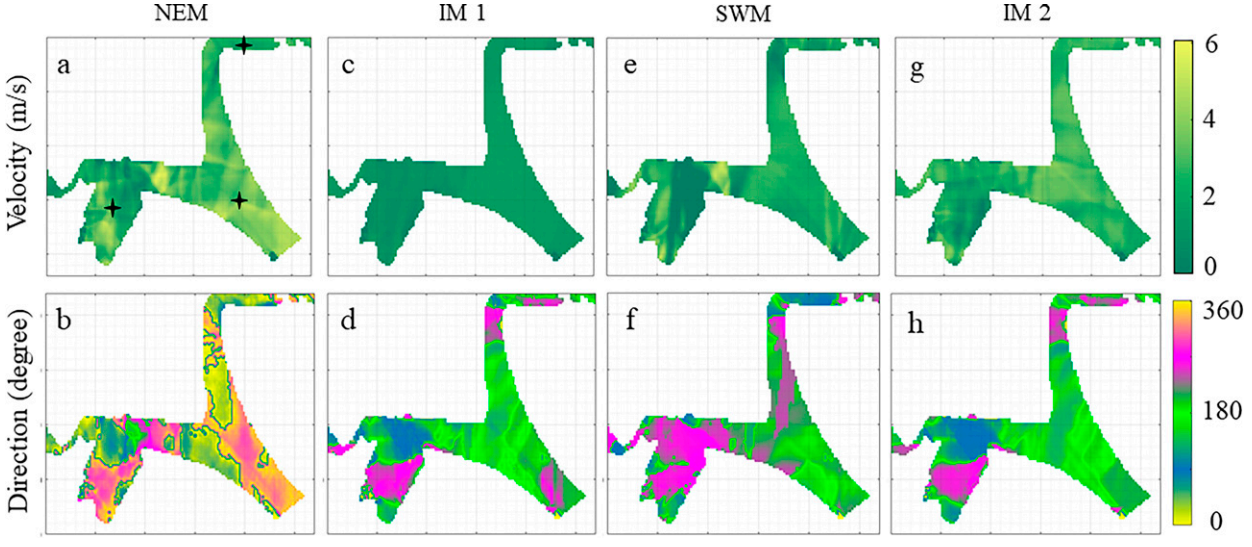

FIG. 10. Wind (top) velocity and (bottom) direction at noon for (a),(b) NEM season (15 Jan 2015); (c),(d) IM (30 Apr 2014); (e),(f) SWM season (1 Aug 2014); and (g), (h) IM (15 Oct 2014) periods. The symbols in (a) indicate the locations of long-term modeling (Fig. 11, below).

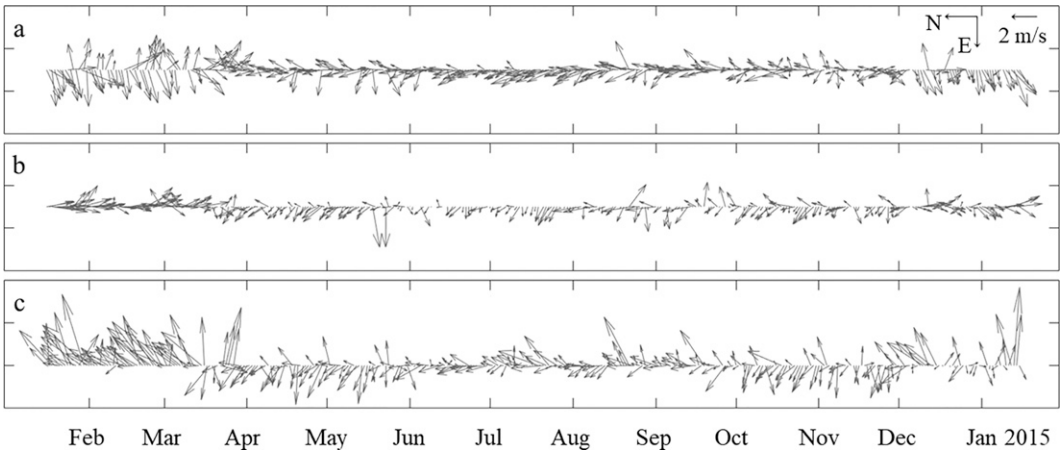

FIG. 11. Long-term modeling results at noon for selected points at the (a) SE limb, (b) SW limb, and (c) NE limb.

than the SW limb. The velocities are higher during the NEM months, which is typical. Wind speeds in the SW limb (Fig. 11b) are markedly lower throughout the year. Although the reduction is more significant in the IM and the SWM seasons, coinciding with periods of relatively weaker winds, the main cause of the reduction in wind speeds is sheltering caused by the tall buildings and structures to the north and south of the SW limb. For the NE limb (Fig. 11c), wind velocities remain relatively high in the NEM season, comparable to the SE limb; however, they generally were lower for the other seasons, especially during the SWM season. This can be attributed to wind-sheltering effects of high-rise apartments to the south of NE limb. The wind direction results at all locations (Fig. 10) show similar consistency with the prevailing wind directions for the SE limb (Fig. 11a) generally being from the north during the NEM season and south during the SWM season. There is greater variability in the wind directions observed for the SW limb and NE limb, because of wind-sheltering effects.

4. Conclusions

Analysis of the measured wind data for a reservoir in downtown Singapore showed that the wind field within the SE limb is consistent with the prevailing wind conditions as this area is relatively free of surrounding structures. Greater variability in the wind field was observed especially for the SW limb, which is surrounded by tall buildings. These structures provide sheltering effects during both the NEM and SWM seasons, resulting in clear alterations to wind direction and changes to wind speed at the measurement locations.

The effects of wind sheltering were predicted by a CFD model, run under steady conditions, using the mean wind speeds measured at the SE limb, chosen as the reference velocity for the input boundary condition. The CFD results revealed the impact that the surrounding structures have in influencing the spatial distribution of the wind field over the reservoir surface, altering the wind direction and wind speed. The sheltering effects are especially significant in the SW limb, where surrounding structures can exert impacts over areas of the reservoir surface due to the proximity of these structures and the relatively small water surface area.

An algorithm was developed to couple the steady CFD model (used to provide the spatial pattern) results and measured wind data (used to provide the temporal pattern). Demonstration of the wind model was performed by running the model for a full year. Snapshots of the model results show that the spatial variation of the wind field for the reservoir is well predicted by the model. Model validation revealed significant seasonal variation of the wind field over the reservoir surface. Incorporating the measured data with the steady CFD results, the developed wind model is therefore able to predict the spatiotemporal pattern of the wind field over the reservoir surface in real time.

Following the conclusion of this study, we have integrated the wind model with a linked catchment and 3D reservoir model. This suite of linked models will enable us to predict, in real time, the impact of wind effects on reservoir water quality in support of better operations and planning decisions (Irvine et al. 2019). Additional future scenarios and lines of research also would be worth pursuing. In particular, sensitivity analysis might be undertaken by comparing the wind fields over the reservoir without the current tall buildings as compared with the existing building configuration. Additional building obstructions also might be modeled to represent future development around the reservoir with results being used to guide building configuration to minimize water quality impacts. Finally, we note that the existing detailed monitoring had excellent time step coverage. However, it would be valuable to both extend the temporal length of record for more rigorous assessment of model uncertainty and conduct additional directed spatial measurements of wind speed especially at the surface of the waterbody. Such measurements would more specifically define sheltering dynamics that might be used to refine the modeling approach.

Acknowledgments. This work is supported by the Singapore National Research Foundation, under its Environment

and Water Technologies Strategic Research Programme and administered by the Environment and Water Industry Programme Office, and PUB, Singapore's National Water Agency, under project 1002-IRIS-09. There is no conflict of interest for this study.

Data availability statement. This paper was thoroughly vetted by the Public Utilities Board (PUB), Singapore's National Water Agency, and approved for submission to peer-reviewed journal and for public release. The data used in this study comprise wind data measured at the sensor locations indicated in the paper. The data belong to the PUB (https://www.pub.gov.sg/). Interested parties are advised to contact the PUB directly for access to the data.

REFERENCES

Alexander, R., and J. Imberger, 2009: Spatial distribution of motile phytoplankton in a stratified reservoir: The physical controls on patch formation. *J. Plankton Res.*, **31**, 101–118, https://doi.org/10.1093/plankt/fbn101.

Anderson, J. D., 1995: *Computational Fluid Dynamics: The Basics with Applications.* McGraw-Hill, 547 pp.

ANSYS, 2019: ANSYS fluent. Accessed 21 July 2019, https://www.ansys.com/products/fluids/ansys-fluent.

Coulibaly, P., and N. D. Evora, 2007: Comparison of neural network methods for infilling missing daily weather records. *J. Hydrol.*, **341**, 27–41, https://doi.org/10.1016/j.jhydrol.2007.04.020.

Daley, R., 1991: *Atmospheric Data Analysis.* Vol. 2, Cambridge University Press, 457 pp.

Dembélé, M., F. Oriani, J. Tumbulto, G. Mariéthoz, and B. Schaefli, 2019: Gap-filling of daily streamflow time series using Direct Sampling in various hydroclimatic settings. *J. Hydrol.*, **569**, 573–586, https://doi.org/10.1016/j.jhydrol.2018.11.076.

Du, W., Z. Xing, M. Li, B. He, L. H. C. Chua, and H. Miao, 2014: Optimal sensor placement and measurement of wind for water quality studies in urban reservoirs. *IPSN-14 Proc. 13th Int. Symp. on Information Processing in Sensor Networks*, Berlin, Germany, IEEE, 167–178.

Gong, R., L. Xu, D. Wang, H. Li, and J. Xu, 2016: Water quality modeling for a typical urban lake based on the EFDC model. *Environ. Model. Assess.*, **21**, 643–655, https://doi.org/10.1007/s10666-016-9519-1.

Google Earth, 2017: Topical reservoir 1 18′38″ N and 103 52′ 00″ E, elevation 1912 m. 3D map, accessed 7 July 2018, https://earth.google.com/web/@1.28882325,103.86420314,3.64901028a,3064.73984592d,35y,0.00000001h,51.50000616t,-0r.

Hendricks, E. A., S. R. Diehl, D. A. Burrows, and R. Keith, 2007: Evaluation of a fast-running urban dispersion modeling system using joint urban 2003 field data. *J. Appl. Meteor. Climatol.*, **46**, 2165–2179, https://doi.org/10.1175/2006JAMC1289.1.

Hipsey, M. R., M. Sivapalan, and T. P. Clement, 2004: A numerical and field investigation of surface heat fluxes from small wind-sheltered waterbodies in semi-arid Western Australia. *Environ. Fluid Mech.*, **4**, 79–106, https://doi.org/10.1023/A:1025547707198.

Hodges, B. R., J. Imberger, A. Saggio, and K. B. Winters, 2000: Modeling basin-scale internal waves in a stratified lake. *Limnol. Oceanogr.*, **45**, 1603–1620, https://doi.org/10.4319/lo.2000.45.7.1603.

Imberger, J., C. Marti, C. Dallimore, D. Hamilton, J. Escriba, and G. Valerio, 2017: Real-time, adaptive, self-learning management of lakes. *37th IAHR World Congress*, Kuala Lumpur, Malaysia, IAHR, 72–86.

Irvine, K. N., T. P. Murphy, T. Tang, L. M. Greer, and D. Walters, 2003: Spatial and temporal trends in chlorophyll a, nutrients, and sediment in relation to avian mortality, Whitewater Lake, Manitoba, Canada. *Sediment Quality Assessment and Management: Insight and Progress*, M. Munawar, Ed., Aquatic Ecosystems Health and Management Society, 271–286.

——, L. H. C. Chua, M. Ashrafi, M. T. Nguyen, and K. X. Chong, 2019: Simulation of water quantity and quality for Marina and Kranji Reservoirs. *Innovation in Water Singapore*, Vol. 11, 29–30, https://www.pub.gov.sg/Documents/Issue%2011_Innovation%20in%20Water,%20Singapore_Full%20PDF.pdf.

Jin, K.-R., and Z.-G. Ji, 2004: Case study: Modeling of sediment transport and wind-wave impact in Lake Okeechobee. *J. Hydraul. Eng.*, **130**, 1055–1067, https://doi.org/10.1061/(ASCE)0733-9429(2004)130:11(1055).

Kangur, K., P. Kangur, K. Ginter, K. Orru, M. Haldna, T. Möls, and A. Kangur, 2013: Long-term effects of extreme weather events and eutrophication on the fish community of shallow Lake Peipsi (Estonia/Russia). *J. Limnol.*, 72, 376–387, https://doi.org/10.4081/jlimnol.2013.e30.

——, K. Ginter, P. Kangur, A. Kangur, P. Nõges, and A. Laas, 2016: Changes in water temperature and chemistry preceding a massive kill of bottom-dwelling fish: An analysis of high-frequency buoy data of shallow Lake Võrtsjärv (Estonia). *Inland Waters*, **6**, 535–542, https://doi.org/10.1080/IW-6.4.869.

Karthikeya, B. R., P. S. Negi, and N. Srikanth, 2016: Wind resource assessment for urban renewable energy application in Singapore. *Renewable Energy*, **87**, 403–414, https://doi.org/10.1016/j.renene.2015.10.010.

Krause, A., C. Guestrin, A. Gupta, and J. Kleinberg, 2006: Near-optimal sensor placements: Maximizing information while minimizing communication cost. *2006 Fifth Int. Conf. on Information Processing in Sensor Networks*, Nashville, TN, IEEE, 2–10, https://doi.org/10.1145/1127777.1127782.

Laval, B., J. Imberger, B. R. Hodges, and R. Stocker, 2003: Modeling circulation in lakes: Spatial and temporal variations. *Limnol. Oceanogr.*, **48**, 983–994, https://doi.org/10.4319/lo.2003.48.3.0983.

Markfort, C. D., A. L. S. Perez, J. W. Thill, D. A. Jaster, F. Porté-Agel, and H. G. Stefan, 2010: Wind sheltering of a lake by a tree canopy or bluff topography. *Water Resour. Res.*, **46**, W03530, https://doi.org/10.1029/2009WR007759.

Marti, C. L., and J. Imberger, 2008: Exchange between littoral and pelagic waters in a stratified lake due to wind-induced motions: Lake Kinneret, Israel. *Hydrobiologia*, **603**, 25–51, https://doi.org/10.1007/s10750-007-9243-6.

——, ——, L. Garibaldi, and B. Leoni, 2016: Using time scales to characterize phytoplankton assemblages in a deep subalpine lake during the thermal stratification period: Lake Iseo, Italy. *Water Resour. Res.*, **52**, 1762–1780, https://doi.org/10.1002/2015WR017555.

Meteorological Service Singapore, 2018: Climate of Singapore. Accessed 15 August 2018, http://www.weather.gov.sg/climate-climate-of-singapore/.

Moss, B., and Coauthors, 2011: Allied attack: Climate change and eutrophication. *Inland Waters*, **1**, 101–105, https://doi.org/10.5268/IW-1.2.359.

Murphy, T., K. Irvine, J. Guo, J. Davies, H. Murkin, M. Charlton, and S. Watson, 2003: New microcystin concerns in the Lower

Great Lakes. *Water Qual. Res. J.*, **38**, 127–140, https://doi.org/10.2166/wqrj.2003.008.

Nourani, V., M. T. Alami, and F. D. Vousoughi, 2016: Hybrid of SOM-clustering method and wavelet-ANFIS approach to model and infill missing groundwater level data. *J. Hydrol. Eng.*, **21**, 05016018, https://doi.org/10.1061/(ASCE)HE.1943-5584.0001398.

Orfanidis, S. J., 1996: *Introduction to Signal Processing.* Prentice Hall, 798 pp.

Podsetchine, V., and G. Schernewski, 1999: The influence of spatial wind inhomogeneity on flow patterns in a small lake. *Water Res.*, **33**, 3348–3356, https://doi.org/10.1016/S0043-1354(99)00035-4.

Randall, D. J., and T. K. N. Tsui, 2002: Ammonia toxicity in fish. *Mar. Pollut. Bull.*, **45**, 17–23, https://doi.org/10.1016/S0025-326X(02)00227-8.

R. M. Young, 2020: Wind Monitor-AQ with 4-20 mA Outputs Model 05305L. R. M. Young Co. Doc., 11 pp., https://www.youngusa.com/wp-content/uploads/2008/01/05305L-9028j29.pdf.

Rubbert, S., and J. Köngeter, 2005: Measurements and three-dimensional simulations of flow in a shallow reservoir subject to small-scale wind field inhomogeneities induced by sheltering. *Aquat. Sci.*, **67**, 104–121, https://doi.org/10.1007/s00027-004-0719-4.

Rueda, F. J., S. G. Schladow, S. G. Monismith, and M. T. Stacey, 2005: On the effects of topography on wind and the generation of currents in a large multi-basin lake. *Hydrobiologia*, **532**, 139–151, https://doi.org/10.1007/s10750-004-9522-4.

Schueler, T., and J. Simpson, 2001: Why urban lakes are different. *Watershed Prot. Tech.*, **3**, 747–750.

Shabalala, Z. P., M. E. Moeletsi, M. I. Tongwane, and S. M. Mazibuko, 2019: Evaluation of infilling methods for time series of daily temperature data: Case study of Limpopo Province, South Africa. *Climate*, **7**, 86, https://doi.org/10.3390/cli7070086.

Stull, R. B., 2017: *Meteorology for Scientists and Engineers.* Brooks Cole, 938 pp.

Tardivo, G., and A. Berti, 2012: A dynamic method for gap filling in daily temperature datasets. *J. Appl. Meteor. Climatol.*, **51**, 1079–1086, https://doi.org/10.1175/JAMC-D-11-0117.1.

Valerio, G., M. Pilotti, C. L. Marti, and J. Imberger, 2012: The structure of basin-scale internal waves in a stratified lake in response to lake bathymetry and wind spatial and temporal distribution: Lake Iseo, Italy. *Limnol. Oceanogr.*, **57**, 772–786, https://doi.org/10.4319/lo.2012.57.3.0772.

Wang, X., Y. Li, K. Wang, X. Yang, and P. W. Chan, 2017: A simple daily cycle temperature boundary condition for ground surfaces in CFD predictions of urban wind flows. *J. Appl. Meteor. Climatol.*, **56**, 2963–2980, https://doi.org/10.1175/JAMC-D-17-0095.1.

Wang, Y., J. Decker, and E. R. Pardyjak, 2020: Large-eddy simulations of turbulent flows around buildings using the Atmospheric Boundary Layer Environment–Lattice Boltzmann Model (ABLE-LBM). *J. Appl. Meteor. Climatol.*, **59**, 885–899, https://doi.org/10.1175/JAMC-D-19-0161.1.

Wu, X., M. Liu, and Y. Wu, 2012: In-situ soil moisture sensing: Optimal sensor placement and field estimation. *ACM Trans. Sens. Networks*, **8**, 33, https://doi.org/10.1145/2240116.2240122.

Xing, Z., L. Chua, H. Miao, J. Imberger, and P. Yang, 2018: Wind shielding impacts on water quality in an urban reservoir. *Water Resour. Manage.*, 32, 3549–3561, https://doi.org/10.1007/s11269-018-1980-y.

Zhu, G., F. Wang, Y. Zhang, G. Gao, and B. Qin, 2008: Hypoxia and its environmental influences in large, shallow, and eutrophic Lake Taihu, China. *SIL Proc.*, **30**, 361–365, https://doi.org/10.1080/03680770.2008.11902144.